







Hot electron retention in laser plasma created under terawatt subnanosecond irradiation of Cu targets

T Pisarczyk¹ , M Kalal^{2,3}, S Yu Gus'kov^{4,5}, D Batani⁶, O Renner^{3,7,8}, J Santos⁶, R Dudzak^{3,8}, A Zaras-Szydłowska¹, T Chodukowski¹, Z Rusiniak¹, J Dostal^{3,8}, J Krasa⁸ , M Krupka^{2,3,8}, Iu Kochetkov⁵, S Singh^{3,8}, J Cikhardt^{3,9} , T Burian^{3,8}, M Krus³, M Pfeifer^{3,8}, G Cristoforetti¹⁰ , L A Gizzi¹⁰, F Baffigi¹⁰, L Antonelli¹¹, N N Demchenko⁴, M Rosinski¹, D Terwińska¹ , S Borodziuk¹, P Kubes⁹ , M Ehret⁶, L Juha^{3,8}, J Skala⁸ and Ph Korneev^{4,5}

¹ Institute of Plasma Physics and Laser Microfusion, Warsaw, Poland

² Faculty of Nuclear Science and Physics Engineering, Czech Technical University in Prague, 115 19, Prague, Czech Republic

³ Institute of Plasma Physics, Czech Academy of Sciences, 182 00, Prague, Czech Republic

⁴ P.N. Lebedev Physical Institute of RAS, 119991, Moscow, Russia

⁵ National Research Nuclear University MEPhI, 115409, Moscow, Russia

⁶ Univ. Bordeaux, CNRS, CEA, CELIA, UMR 5107, F-33405, Talence, France

⁷ ELI Beamlines, Institute of Physics, Czech Academy of Sciences, 252 41, Dolni Brezany, Czech Republic

⁸ Department of Radiation and Chemical Physics, Institute of Physics, Czech Academy of Sciences, 182 21, Praha, Czech Republic

⁹ Faculty of Electrical Engineering CTU, 166 27, Prague, Czech Republic

¹⁰ National Institute of Optics, CNR, Pisa, Italy

¹¹ York Plasma Physics Institute, University of York, York, United Kingdom

E-mail: tadeusz.pisarczyk@ifpilm.pl

Received 26 May 2020, revised 28 August 2020

Accepted for publication 10 September 2020

Published 5 October 2020



CrossMark

Abstract

Laser plasma created by intense light interaction with matter plays an important role in high-energy density fundamental studies and many prospective applications. Terawatt laser-produced plasma related to the low collisional and relativistic domain may form supersonic flows and is prone to the generation of strong spontaneous magnetic fields. The comprehensive experimental study presented in this work provides a reference point for the theoretical description of laser-plasma interaction, focusing on the hot electron generation. It experimentally quantifies the phenomenon of hot electron retention, which serves as a boundary condition for most plasma expansion models. Hot electrons, being responsible for nonlocal thermal and electric conductivities, are important for a large variety of processes in such plasmas. The multiple-frame complex-interferometric data providing information on time resolved spontaneous magnetic fields and electron density distribution, complemented by particle spectra and x-ray measurements, were obtained under irradiation of the planar massive Cu and plastic-coated targets by the iodine laser pulse with an intensity of above 10^{16} W cm⁻².



Original content from this work may be used under the terms of the [Creative Commons Attribution 4.0 licence](https://creativecommons.org/licenses/by/4.0/). Any further distribution of this work must maintain attribution to the author(s) and the title of the work, journal citation and DOI.

The data shows that the hot electron emission from the interaction region outside the target is strongly suppressed, while the electron flow inside the target, *i.e.* in the direction of the incident laser beam, is a dominant process and contains almost the whole hot electron population. The obtained quantitative characterization of this phenomenon is of primary importance for plasma applications spanning from ICF to laser-driven discharge magnetic field generators.

Keywords: hot electrons, laser plasma, plasma, complex interferometry, polarimetry

(Some figures may appear in colour only in the online journal)

1. Introduction

Under the action of intense laser radiation above 10^{13} – 10^{15} W cm⁻² matter instantly ionizes to a plasma state and behaves as a medium of charged particles. As it is normally neutral on the spatial scales above the Debye length, it can contain spatially distributed magnetic fields. The generation of those so-called spontaneous magnetic fields (SMF) is associated with currents of various origins in nonequilibrium laser-produced plasma. This is one of the most important phenomena accompanying the interaction of the intense laser radiation with matter. It affects many aspects of plasma behavior, modifying transport of charged species, spatial and temporal distributions of their density and temperature, and defining the physics of the interaction processes.

First reported in [1, 2], SMF generation is being actively studied both theoretically and experimentally. A number of mechanisms relevant to different interaction parameters were discussed, such as the generation of thermoelectric currents produced by crossed gradients of plasma temperature and density [2, 3]; the generation of strong currents of hot electrons by resonance laser energy absorption [4, 5]; and the development of parametric instabilities [6]. Generally, the physics under these mechanisms may vary from being primarily of a hydrodynamic or kinetic nature, with the kinetic effects becoming more important for higher intensities [7]. The full description of the interaction process is, however, rather challenging. In this context, the SMF in the expanding plasma may give an insight into the electron currents generated inside the plasma, and related to those escaping outside the interaction region.

It is evident that SMF generation is associated with the generation of fast electrons. The experimental observation of hot electrons at the Prague Asterix Laser System (PALS) facility at a laser intensity of around 3×10^{16} W cm⁻² showed significant discrepancies between electron temperatures in this and other subrelativistic and ultrarelativistic intensity experiments. Scaling laws derived from various models indicated that these discrepancies could be ascribed to the self-focusing of the laser beam in coronal plasma which increases the original nonrelativistic laser intensity to an adequate relativistic value [8]. Also, experimentally observed values of maximum proton energy reaching values up to 5 MeV correlate with this conclusion. The occurrence of other nonlinear forces in laser pulse interaction with generated plasma was also observed, as surveyed in [8].

During the plasma expansion into the vacuum, a part of the electrons is accelerated to energies much above the average, and a small part of them can leave the plasma, causing the slower plasma and thus the target to be positively charged [9]. The total number of escaping electrons is defined by dynamical competition between the high energy of escaping electrons and the electric potential increase due to the electron escape [10]. The resulting target potential Φ could be larger than the characteristic energy of electrons given by the temperature T_h of hot electrons: $\Phi \gtrsim T_h/e$, where e is the elementary charge [11]. The separation of charges results in the creation of a double layer, where the resulting potential divides electrons into free and trapped (or reflected) [12]. If the target is grounded then its positive charge may be gradually neutralized by a return target current flowing from the ground. Then the target potential is established by a balance between the rate of electron ejection and the amplitude of the return current flowing through the target holder. The low energy electrons supplied by the grounded target holder to the plasma are subjected to thermalization in order to fill vacancies in the energy distribution function [13].

It is generally assumed that the trapped electrons transfer a part of their energy to ions, which are thus accelerated. As a result, the trapped electrons should have low energy and the number of fast electrons should decrease. However, the use of a multifaceted diagnostic of laser-produced plasma, which made possible the estimation of the number of hot electrons produced by laser-plasma interactions, revealed significant differences between the individual diagnostics. The measurement of the electron distribution functions gave a surprisingly low number of hot electrons ($\sim 10^9$), compared to the number of electrons needed to accelerate a number ($\sim 10^{14}$) of the MeV deuterons in the direction opposite to the laser beam propagation [8]. A difference of several orders of magnitude probably indicates that the hot electrons are partially retained in the plasma by a hitherto unaccounted mechanism. A similar difference was also found when comparing the number of electrons delivered to the neutralization of the positive charge of the target [14]. Even in this case, it is certainly a complex process of electron escape from the plasma and their simultaneous reflection into the plasma, as evidenced by the long discharge time, which is much longer than the duration of the laser-plasma interaction, as has been experimentally demonstrated for laser intensities ranging from 10^9 to 10^{16} W cm⁻² [13, 15]. In addition, the experimentally observed return currents neutralizing the target reached a maximum value of only

a few kA [16] compared to the currents reaching a value up to 800 kA, which were calculated from the magnetic field and electron density distribution observed inside the plasma [7]. This again indicates that most of the hot electrons could be retained in the plasma. These facts suggest that some phenomena have hitherto not been covered by the theory.

Plasma expansion strongly depends on electron energy distribution. Roughly, in the 1D approach, the density and velocity profiles of the expanding plasma are defined by models proposed in [17, 18]. However, the discussed question of the boundary condition on the expanding plasma edge is beyond the 1D approach. The 1D approach may be valid at the initial time, when the expansion distance is less than the scale of a transverse inhomogeneity, e.g. the focal spot size. There, the plasma potential linearly grows up, which in the 1D model would prevent an electron current at large distances, so that no electrons would be registered in distant spectrometers, contradicting observations. In a real situation, the current and electron distribution is defined by the 3D potential barrier height. Experimental characterization of the number of escaping electrons, *i.e.* in a model approach, the electron currents at the distances, where 1D expansion switches to the 3D one, and their correlation with the internal currents in the expanding plasma is the main goal of the paper.

The experimental study presented in this work was performed at the PALS [19]. The main diagnostics used benefits from the application of a three-frame complex interferometer driven by an auxiliary Ti:Sa femtosecond laser, an upgraded version of that reported in [20]. This unique tool provides time-dependent information on the laser plasma density and the SMF distributions with micrometer-scale spatial and femtosecond-scale temporal resolution. The optical diagnostic technique is based on the amplitude-phase analysis of complex interferograms [20–22], the information on both the density and magnetic field distributions are collected at a given moment by a common channel. In order to obtain a description of the hot electron distribution that is as detailed as possible, massive and layered Cu targets (massive Cu coated by different thickness layers of plastic) were used, facilitating an application of the 2D imaging of the $K\alpha$ line emission from Cu. Data on spatial distribution of the hot electrons emitted outside the interaction region was obtained using the multi-channel magnetic electron spectrometer. The complex collected data map the SMF distribution, determine the hot electron currents inside the expanding plasma, and relate them to the outside emitted fast electron spectra. Their analysis sheds new light on the phenomenon of the hot electron retention and provides a boundary condition for the plasma expansion models.

2. Experimental setup

The ablative expanding plasma was produced from massive flat targets made of Cu (in the shape of a cuboid with dimensions of $5 \times 5 \times 50$ mm) irradiated by the linearly (vertically) polarized PALS iodine laser beam at the main frequency (1315 nm), with the pulse duration of about 350 ps at the

FWHM and energy of ~ 500 J. It was focused to the focal spot of $\sim 100 \mu\text{m}$ in diameter, normal to the target surface, providing the intensity level on the target up to $2 \cdot 10^{16} \text{ W cm}^{-2}$, as schematically shown in figure 1.

Figure 1 illustrates the location of principal diagnostics used, the target structure and the temporal and spatial intensity distribution of the unfocused laser beam. One of the key diagnostics was the three-frame complex interferometric system which provides information on SMF and electron density distributions in the expanding plasma. The ten-channel array of magnetic electron spectrometers characterized the energy distribution of electrons emitted from the target at different angles with respect to the incident laser beam direction. Finally, the 2D x-ray imaging system showed the hot electron distribution inside the dense target based on detection of the Cu $K\alpha$ line emission diffracted on the spherically bent quartz crystal.

2.1. Three-frame polaro-interferometric system

To obtain information about space-time distributions of SMF and electron density, the three-frame polaro-interferometer shown in figure 2 has been implemented. This system consisted of three independent channels, modified for operating in the complex-interferometry regime [19, 23]. In accordance with the general ideas described in [19], in order to obtain a complex interferogram the analyzing polarizer (analyzer) must be rotated by a suitable (usually quite small, $\sim 2^\circ$ in this setup) angle away from the direction perpendicular to the input polarizer. The three complex interferograms were separated by a time delay of ~ 400 ps by an optical delay line. The polaro-interferometer was driven by a Ti:Sa femtosecond laser with FWHM pulse duration of 40 fs and energy of 10 mJ. The temporal position of the initial frame was adjusted to the maximum intensity of the main laser pulse. The PALS and Ti:Sa laser pulses were synchronized with accuracy ± 100 ps by the method of electronic synchronization described in [24]. The interferograms were registered by high-resolution CCD cameras driven by the GigEV protocol and controlled by a custom-built application PALS Vision GigEV [25]. The algorithm of the optical data analysis is presented in [19, 26].

2.2. Ten-channel magnetic electron spectrometer

The parameters of hot electrons emitted from the interaction region were obtained by a ten-channel magnetic electron spectrometer, as shown in figure 3.

Each module consists of a permanent ferrite or neodymium magnet, magnetically soft steel poles, lead shield and plastic aperture inserted in a brass block. It covers electron energies in the range of 50 keV–1.5 MeV or 0.25 MeV–5 MeV, depending on used magnets. The ten-channel spectrometer covered the total angle of approximately 130 degrees, see figure 3. The electron spectrometer on the axis was placed in the beam path at a distance 48 cm from the target. Spectrometers placed outside the focusing beam were placed at a distance of 30 cm from the target. In front of the focusing lens, a rectangular metal mask was placed, shadowing the electron spectrometer from

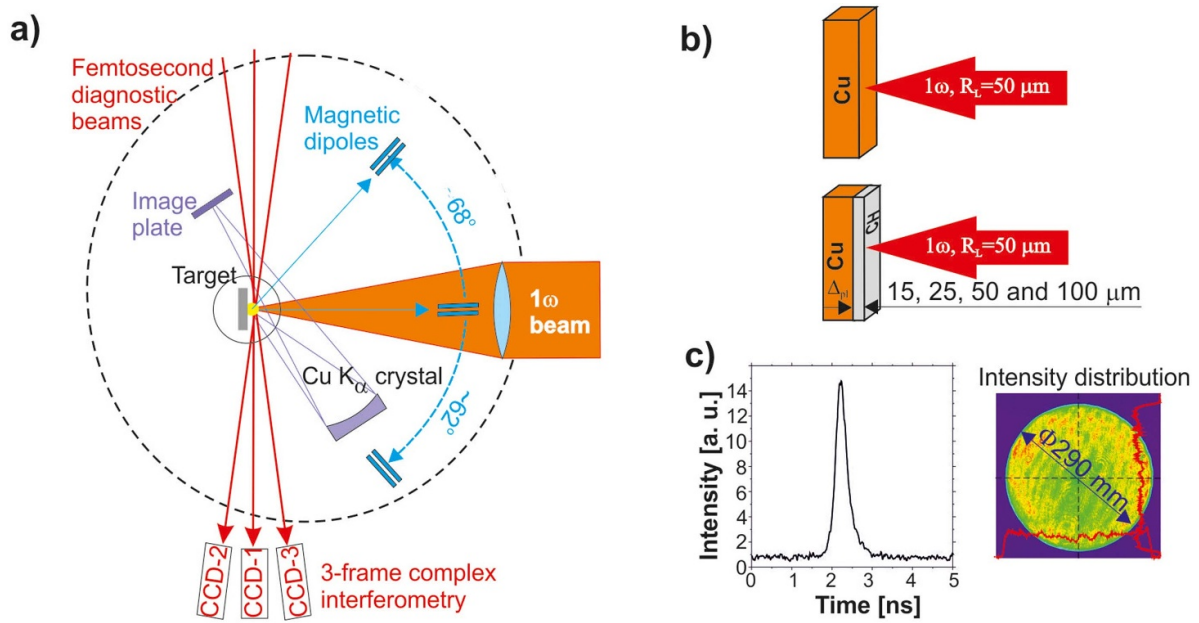


Figure 1. Experimental setup: (a) scheme of diagnostics location in experimental chamber, (b) single and double layer targets irradiation, and (c) temporal profile of the 1ω iodine laser beam and intensity distribution in its cross section.

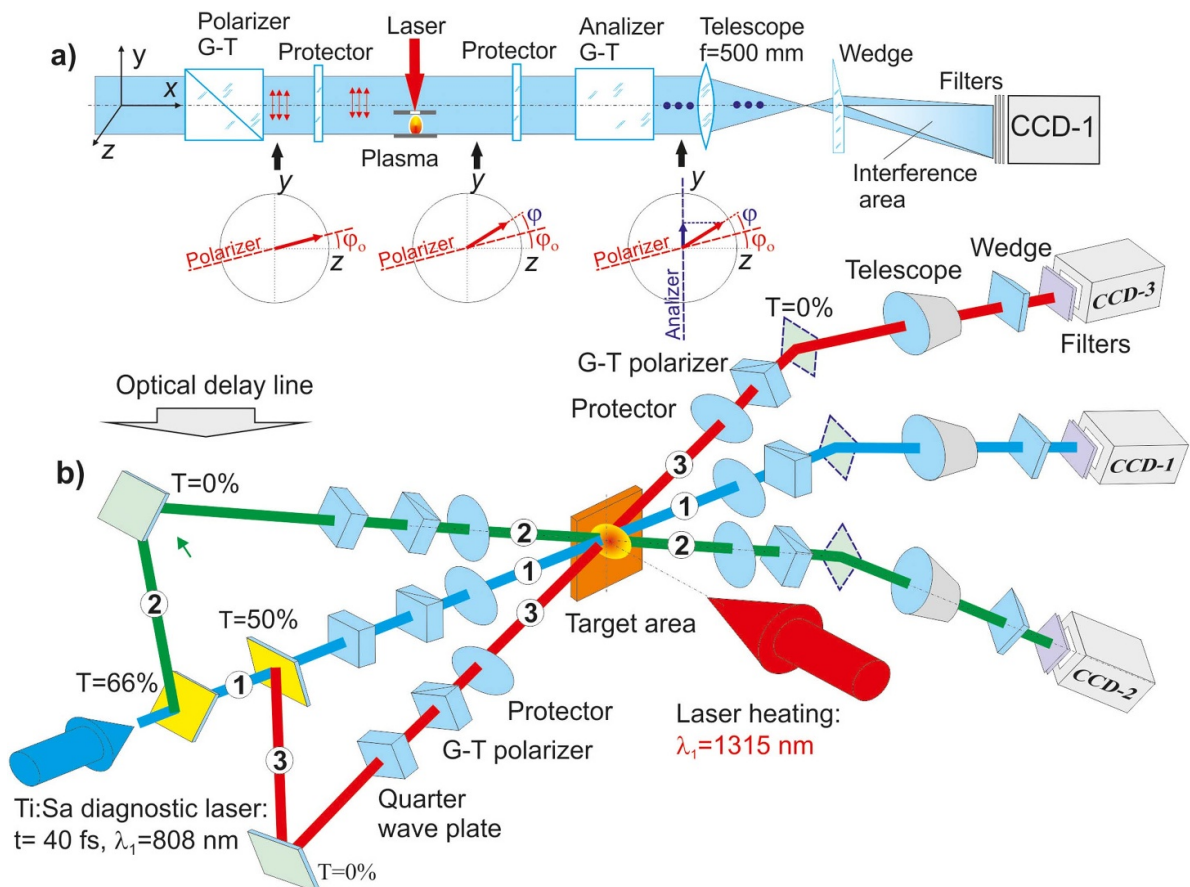


Figure 2. The three-frame complex interferometric system: (a) the optical scheme of the module operating in complex-interferometry mode, and (b) the scheme of the radiation splitting to individual interferometric channels illustrating the space-time separation of frames.

the infrared laser beam. The effect on the focal spot size was minimized by the use of a phase randomizing plate, smoothing

out the beam profile in the focus. Electron fluxes were recorded by the image plates located on the top of the magnetic

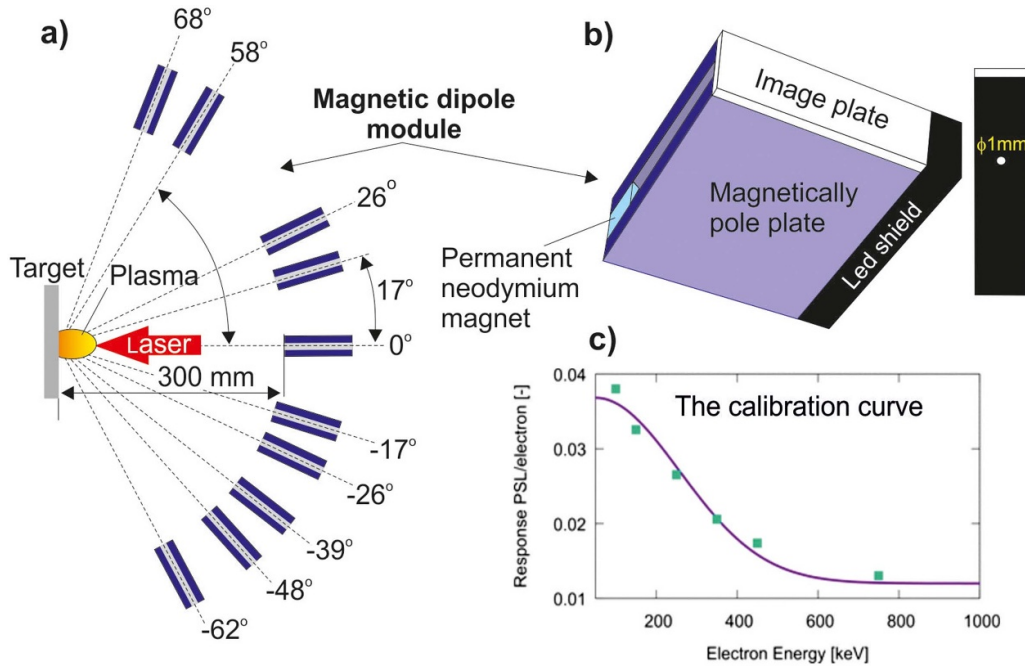


Figure 3. Ten-channel magnetic electron spectrometer: (a) location of the dipole magnet array in the experiment, (b) the construction of individual magnetic dipole modules and (c) the calibration curve.

dipole module (see figure 3(b)). Based on the calibration of the spectrometer energy range and the imaging plate response function (see figure 3(c)), and given the distance and aperture diameter, absolute electron energy spectral density was obtained.

2.2. 2D imaging of the K_{α} line emission from Cu

The 2D x-ray (Cu K_{α}) imaging system with the spherically bent crystal of quartz was applied for the characterization of the total population and energies of hot electrons propagating into the dense material of the target from the irradiated region [23]. The experimental setup is shown in figure 4 and benefits from a near-coincidence of the quartz crystal (422) interplanar spacing $2d = 0.15414$ nm with the wavelength of the hot-electron-induced K_{α} emission (0.15406 nm) from the Cu target.

This results in a quasi-normal incidence configuration of the imaging system with the central Bragg angle $\theta_B = 88.15^\circ$ and consequently in a small distortion of 2D-resolved images mapping the hot electron interaction with the cold target material [26]. The magnified images ($M = 1.73$) of the Cu K_{α} emission from hot electron-affected areas of the substrate were observed at the angle of $\psi = 46^\circ$ (in the horizontal plane) from the surface of the laser-irradiated flat targets. The images were recorded using the absolutely calibrated imaging plates Fuji BAS MS and SR, the signal distribution on exposed plates was mapped using the Fujifilm BAS 1800 scanner with the pixel size $50 \times 50 \mu\text{m}^2$. With respect to the given magnification of the imaging system and the angle of Cu K_{α} observation, this pixel size corresponds to the area of $40.2 \times 28.9 \mu\text{m}$ (horizontal \times vertical direction) on the source. The conversion efficiency of the laser light into hot electrons was determined

from the quantitative evaluation of images taken on bare Cu targets, whereas to determine the energy of the hot electrons, the Cu targets coated with different thickness layers of the CH plastic ($\Delta_{pl} = 15, 25, 50$ and $100 \mu\text{m}$) were used. The details on the evaluation procedure can be found below and in [22, 26].

3. Experimental results

A number of three-frame sequences of raw complex interferograms was obtained for the interaction of the laser beam with an energy of about 500 J with the Cu planar massive target (figure 1(b)). The full set of interferograms, obtained in the experiment and used for the detailed analysis, covered the range from $t = -200$ ps up to about $t = 1000$ ps related to the laser pulse maximum. Figure 5 shows an example of four complex interferograms selected from three-frame sequences that were taken in three shots of the iodine laser. These complex interferograms correspond to the characteristic stages of the plasma expansion time, namely: before the maximum laser intensity ($t = -108$ ps), around its maximum ($t = 19$ ps), before ($t = 226$ ps) and after the end ($t = 449$ ps) of the laser pulse. All complex interferograms exhibit an antisymmetry related to the combination of the Faraday effect with the initial rotation of the analyzing polarizer. The brightening is noticeable in the upper half of the expanding plasma. Here the rotation direction of the probe beam polarization is consistent with the direction of the initial rotation of the analyzing polarizer from the orientation perpendicular with respect to the input polarizer. In contrast, the darkening in the lower part of the expanding plasma occurs due to the rotation of the diagnostic beam polarization in the opposite direction. This observation

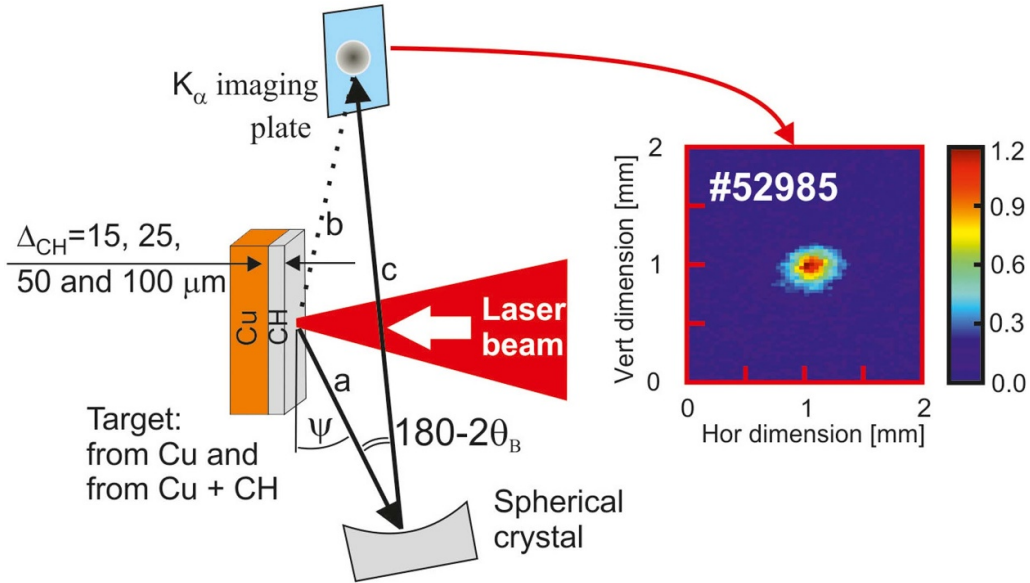


Figure 4. Scheme of the hot electron diagnostic based on 2D x-ray imaging of Cu K α emission and an example of the measured data showing the hot electron distribution along the target surface.

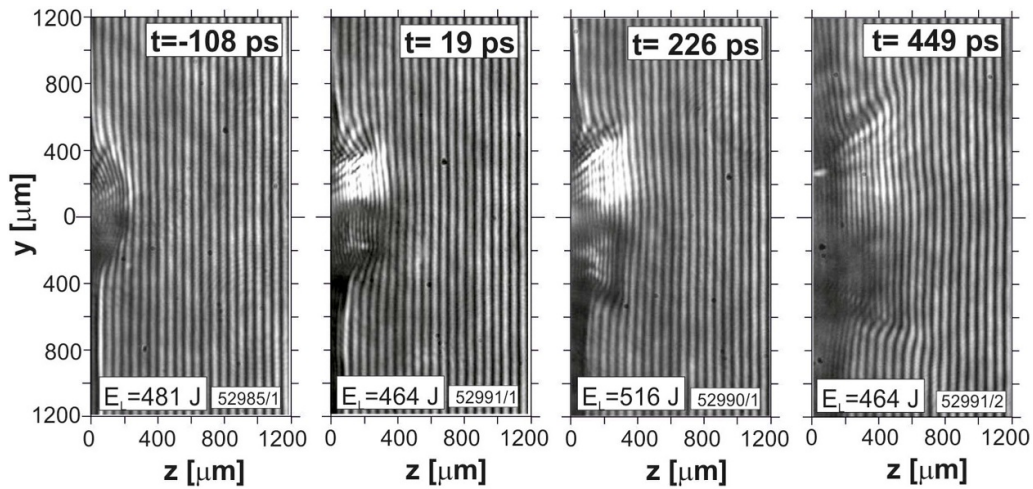


Figure 5. Four complex interferograms selected from three-frame sequences that were taken in three shots of an iodine laser beam delivering energy of about 500 J to planar massive Cu targets. The moment of shooting, t , is related to the peak intensity of the laser pulse.

is consistent with the physically expected azimuthal structure of SMF distribution with respect to the target normal.

The registered interferograms demonstrate virtually axial symmetry of the expanding plasma, enabling calculation of the SMF distributions using for the Faraday rotation angle (φ) and the phase (δ) distributions by Abel equation [26]:

$$\varphi(y) = 5.24 \cdot 10^{-17} \cdot \lambda^2 \int_y^R \frac{B_\varphi(r) n_e(r) dr}{\sqrt{r^2 - y^2}} \quad (1)$$

$$\delta(y) = 8.92 \cdot 10^{-14} \cdot \lambda \int_y^R \frac{n_e(r) r dr}{\sqrt{r^2 - y^2}} \quad (2)$$

where: $B_\varphi(r)$ is the azimuthal magnetic field distribution, $n_e(r)$ is electron density distribution, λ is the wavelength of a probe beam. In accordance with [26], the distribution of the SMF is

determined by the expression:

$$B_\varphi(r) = \frac{1.7 \cdot 10^3}{\lambda} \cdot \left[\frac{r f_B(r)}{f_n(r)} \right], \quad (3)$$

where: $f_n(r) = 4.46 \cdot 10^{-14} \cdot \lambda R n_e(r)$ and $f_B(r) = 2.62 \cdot 10^{-17} \cdot \lambda^2 R \left[\frac{B_\varphi(r) n_e(r)}{r} \right]$ are determined by the Abelization of the phase distribution $\delta(y)$ and the normalized rotation angle distribution $\varphi(y)/y$ respectively. Distributions of phase $\delta(y)$ and the normalized rotation angle $\varphi(y)/y$ are extracted from the data according to the methodology described in [20–22]. The information extraction procedure is based on the analysis of the spectrum of the interferograms after using the 2D Fourier transform and takes into account that the intensity distribution of the complex interferogram contains information about a distribution of amplitude $\gamma(y, z)$ of the probing laser beam while the shift of interferometric fringes

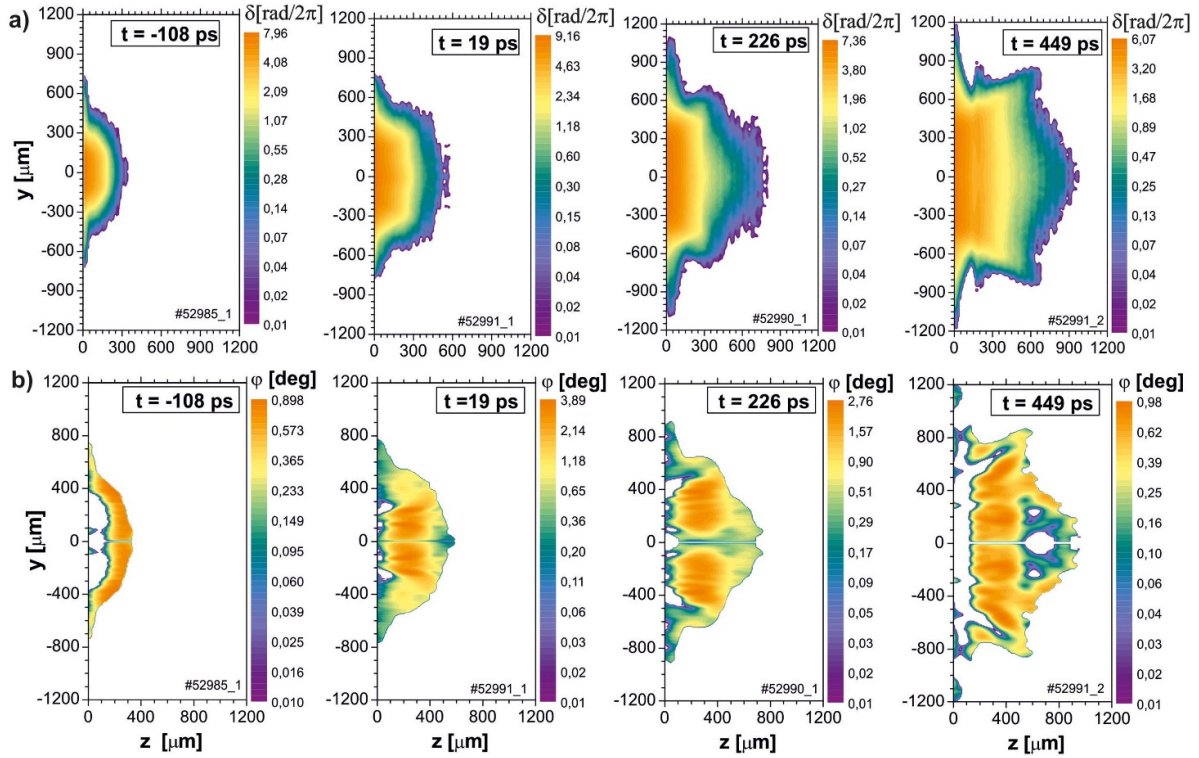


Figure 6. Distribution of the phase (a) and the rotation angle (b) obtained from Fourier analysis based on the selected complex interferogram from figure 5.

$\delta(y, z)$ depends on the phase shift distribution of the diagnostic beam. Then the distribution of Faraday rotation angle is $\varphi(y, z) = \arcsin(\gamma(y, z) \cdot \sin \varphi_0)$, where φ_0 is the initial angle of the rotation of the polarizer (see figure 2(a)). Calculated distributions of phase $\delta(y, z)$ and the rotation angle $\varphi(y, z)$ corresponding to the characteristic moments of the ablation plasma expansion are presented in figure 6, while figure 7 shows the electron density $n_e(r, z)$ and the azimuthal magnetic field $B_\varphi(r, z)$ resulting from these distributions.

The quasi-spherical nature of the ablative expansion of the plasma occurring in the early phase (-108 ps) of the laser-plasma interaction is shown in figure 7(a) by the spatial distribution of the electron density. Later on, a directional disparity appears and evolves with time, see figure 7(a) for 19, 226, and 449 ps, which may be related to diverse mechanisms including plasma instabilities, SMF pressure gradient, and partially also a nonideality of the irradiation process.

Regarding SMF distributions, figure 7(b), they are characterized by the maximum magnetic field values on the plasma front in the area near the symmetry axis. The amplitude reaches the value of 9 MGs in the early phase of plasma expansion ($t = -108$ ps) when the laser intensity increases and then decreases after passing its maximum. A similar structure is maintained until the end of the pulse. At the end of the pulse, the SMF amplitude decreases to about 2 MGs (for $t = 449$ ps) due to the radial expansion of the plasma and the weakening of the SMF generation mechanisms. In this context, an important issue is the accuracy of the data obtained. A deviation in symmetry, which is inevitable in experimental data, leads to an error of about 5%–10% for the extracted phase

and rotation angle distributions, used to obtain information about the SMF with equation (3). The assumption of the axial symmetry works in this procedure as an uncertainty factor, mainly in the central region, thus increasing the error in the magnetic field near the axis to $\pm 20\%$ – 30% [19].

For the present study, the exact distribution of the SMF is not critical. It was verified that the integral current of hot electrons is not sensitive to the detailed distribution of the SMF, but rather to the total magnetic field flux. The latter is an integral value, for which the thin axial region is too small to have a significant effect. Note that calculated in this way, the current includes all the magnetic field sources, including hot electrons, thermo-currents, etc. The current density distributions $j_T(r, z)$ were calculated using the Ampère law [7] based on the obtained SMF distributions, see figure 8(a).

The calculated currents were artificially separated into currents of electrons flowing from the target, *i.e.* direct currents $j_T < 0$, and backflowing from the edge of the plasma bulk to the target, *i.e.* return currents $j_T > 0$ [7]. Figure 8 shows that the maximal current density connected to the emission of electrons from the target is located near the axis and can reach values larger than 10^{14} A m $^{-2}$. Such current density values correspond to the electrons with energies of several tens or even hundreds of kiloelectronvolts recorded by the spectroscopic $K\alpha$ measurements presented below.

To link these current density distributions with the $K\alpha$ emission, distributions of the integrated current along z -axis in different times were calculated using the relationship:

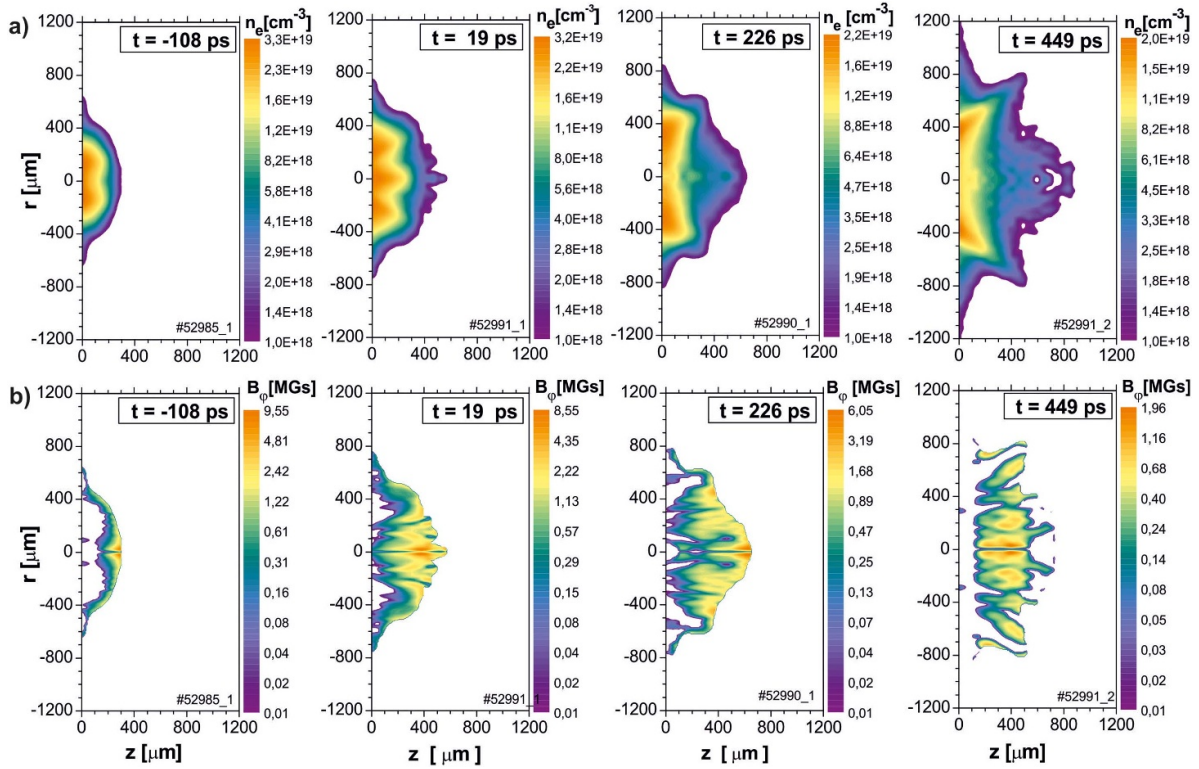


Figure 7. Electron density distributions (a) and the distributions of SMF (b).

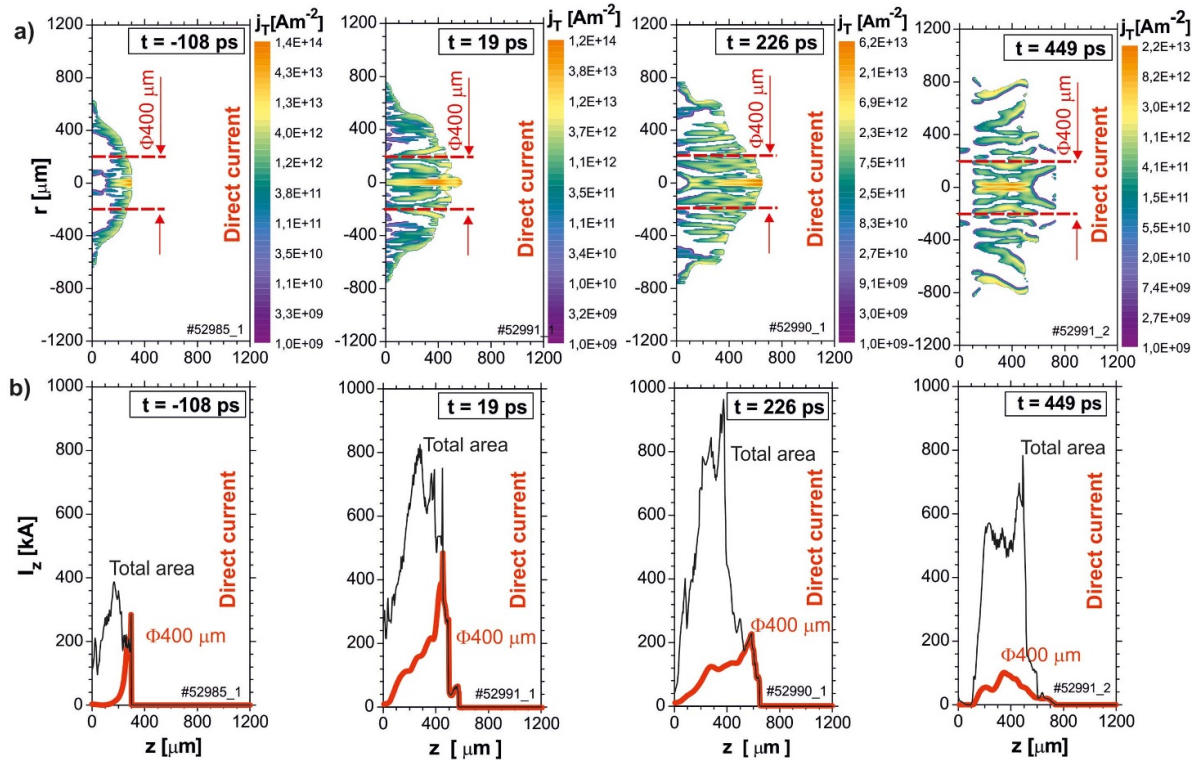


Figure 8. Time-dependent distributions of the direct current density flowing from target surface to the plasma edge (a) and the direct total current calculated based on the azimuthal magnetic field distributions from figure 7. The central plasma diameter $\Phi = 400 \mu\text{m}$ is associated with the size of the K_{α} emitting area, see figure 9.

$I_z(z) = 2\pi \int_0^R j_z(r, z) r dr$ with a finite R . Figure 8(b) shows the total current ($R = \infty$), and the current in the central region of

$400 \mu\text{m}$, which corresponds to the characteristic size of the K_{α} signal, see figure 9.

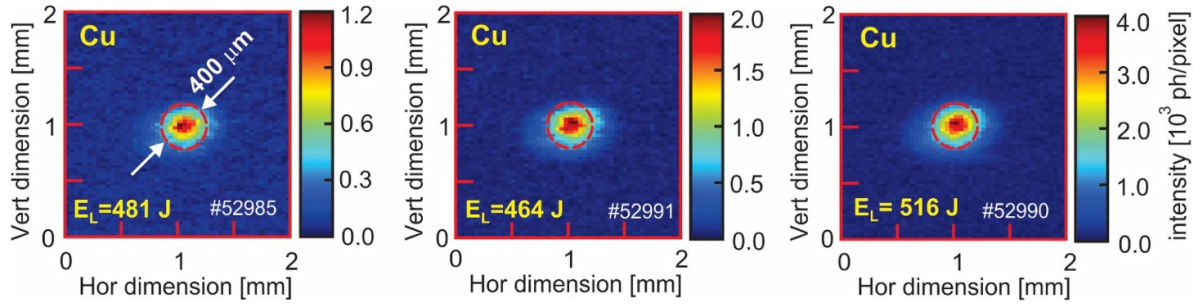


Figure 9. Dimensions of spots characterizing the area of the fast electron interaction with the target material as visualized by $K\alpha$ imaging, for shots from figure 5.

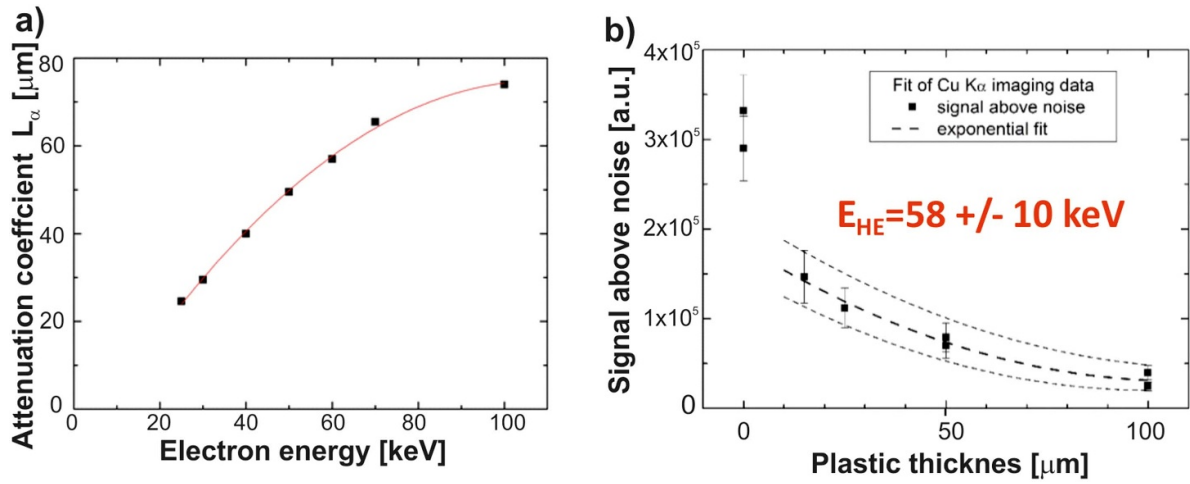


Figure 10. Dependence of the attenuation coefficient L_a on the hot electron energy (a) and exponential fit of experimental data as a function of the plastic thickness layered on massive Cu targets (b).

The direct and return currents in the expanding plasma reconstructed with the use of SMF distributions form closed circuits only if the magnetic field outside the plasma region is absent. The low density in the edge plasma regions does not allow to determine the magnetic fields with a sufficient accuracy [22]. Consequently, the optical diagnostics provide a reliable value for the currents in the dense plasma volume and underestimate currents at larger radial distances, which mainly relate to the return currents. It means that these return currents are partly nonobservable in this type of diagnostics, but they significantly reduce the number of electrons escaping from the target, as observed using electron spectrometers reported below. From figure 8 we can conclude that there is a current of electrons in the direction from the target, containing $\sim 10^{15}$ electrons, which may be to some extent closed by the partly nonobservable return current in the opposite direction, and likely distributed further from the plasma axis. Considering the nature of the observed currents, we may refer e.g. to [7], where they were ascribed mainly to nonthermal kinetic electrons.

We can estimate the total amount of the return hot electrons, propagating within the plasma in the direction ‘to’ the target, using the 2D imaging data of the $K\alpha$ line emission from Cu. To obtain the data information on conversion efficiency of the laser energy to hot electrons and their characteristic energy

Table 1. The laser energy conversion to hot electron energy for different shots with copper targets.

Shot #	E_L (J)	Signal	HE dose (J)	Conversion (%)
52 985	481	1.72E5	2.87	0.6
52 986	479	2.90E5	4.84	1.01
52 989	458	7.99E5	13.3	2.90
52 990	516	5.871E5	9.81	1.90
52 991	464	2.45E5	4.07	0.88
52 992	452	2.16E5	3.61	0.80

from the $K\alpha$ imaging, the massive targets of bare copper and those coated with different thickness plastic layers were used. It should be noted that the conversion efficiency is determined by using bare Cu-massive targets whereas copper coated with different thickness plastic layers were used only to determine hot electron energy. The $K\alpha$ intensities detected as a function of the plastic layer thickness were fitted with the exponential function $I(x) = A \exp(-x/L_a)$ where: A is the fitting constant, x the thickness of the plastic layer and L_a the attenuation coefficient. The values of L_a in dependence on the hot electron energy were derived from the Monte Carlo simulations performed with the Penelope code [26], the computed values fitted using the second degree polynomial are plotted in figure 10(a). The spatially integrated signals in Cu $K\alpha$ images

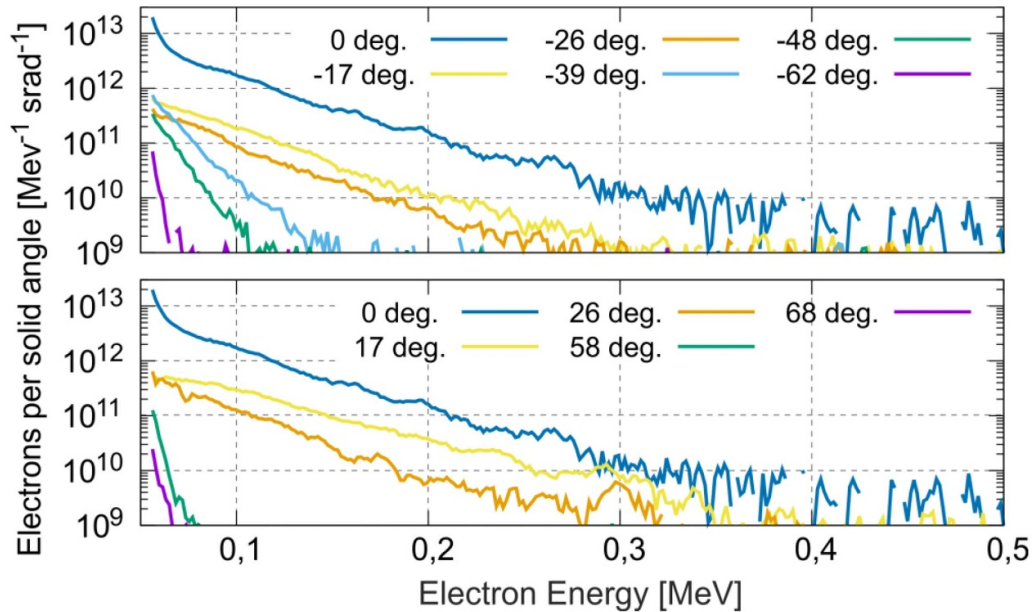


Figure 11. Energy spectra of electrons emitted at different angles vs a normal to the front target surface.

recorded by laser-irradiating the bare and plastic-coated Cu substrates are depicted in figure 10(b).

Their best fitting using the above defined exponential function provided the hot electron energy of 58 ± 10 keV (cf thick best-fit central line and thinner dashed lines corresponding to the defined energy uncertainty in figure 10(b)). We note that this energy was derived from the x-ray signals observed in the emission of targets coated with a 15–100 μm thick plastic layer. More details on the experimental approach and data evaluation procedure can be found e.g. in [27–29].

Quantitative analysis of the $K\alpha$ -emission data show that about 0.6%–3% of the laser energy converts to the energy of hot electrons, propagating from the interaction region in the expanding plasma to the target bulk, see table 1. Fluctuations in conversion efficiency correlate with experimentally observed shot-to-shot fluctuations, which are also independent of deposited laser energy for other plasma parameters.

The recorded Cu $K\alpha$ images shown in figure 9 indicate that a prevailing part of energetic electrons is distributed in the central $\Phi 400$ μm region. The observed dose of hot electrons is comparable with currents deduced from the optical data which give a similar amount of hot electrons in the central region. The electrons outside of this region are probably not energetic enough to generate an observable signal. Some of the hot electrons, with energies exceeding the electrostatic barrier of the charged target, may leave the expanding plasma plume. The number of these electrons is determined from the multichannel spectrometer data, presented below.

These electron fluxes were measured by ten electron spectrometers positioned around the target at a distance of 30 cm. The data obtained in a typical laser shot is presented in figures 11–13. Figure 11 shows the electron energy spectra emitted at different angles of observation for the shot 52 991. The method of their extraction from spectrograms is described in [30]. The strongest electron flux is emitted for all energies

in the direction normal to the target surface, the energy extent of the spectra significantly depends on the emission angle. The energy of electrons emitted in the normal direction reaches the value of several hundreds of keV and the electron temperatures obtained with exponential fitting are shown in figure 12.

Figure 13 shows an angular distribution of different-energy electrons extracted from individual electron spectrometer channels for the shot 52 991. Based on electron energy spectra (cf figures 12 and 13), we present in table 2 the total number of hot electrons escaped from the plasma and average electron currents at a large distance from the target. These currents were estimated from the ratio of the total charge collected by electron spectrometers to the laser pulse duration (350 ps).

The total charge was calculated by interpolating the measured angular distribution of the electron flux over full solid angle assuming the symmetry in the axial direction. As follows from table 2, the number of hot electrons escaping the plasma into the vacuum is much smaller than the number of hot electrons returning to the target. The comparison of the total number of hot electrons in the expanding plasma and outside it shows that the number of electrons overcoming the electrostatic potential and leaving the plasma plume is less than 0.5% of the total number of hot electrons.

4. Interpretation of experimental results

Obviously, the results of all three diverse diagnostics used for the characterization of hot electrons, namely the polaro-interferometric, electron spectrometers, and $K\alpha$ data, need to be agreed within frames of one common model of the plasma expansion. The number of electrons participating in the excitation of the magnetic fields (polaro-interferometry) and in the $K\alpha$ -signal are in quantitative agreement. This agreement indicates that the number of hot electrons returning to the target

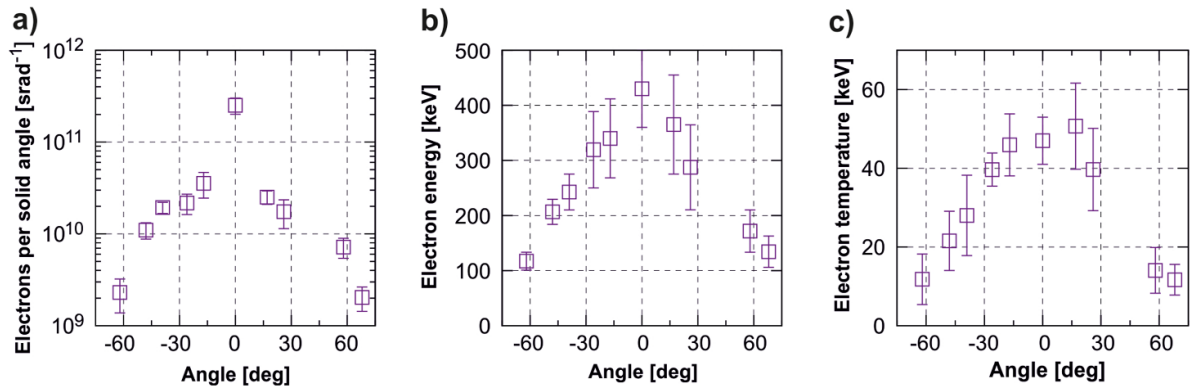


Figure 12. Quantitative analysis of electron energy distribution for solid copper shots: (a) a total electron number emitted into the unit solid angle, (b) highest detected electron energy based on the value where the signal becomes indistinguishable from the noise and (c) temperature of hot electrons obtained by exponential electron energy distribution fitting.

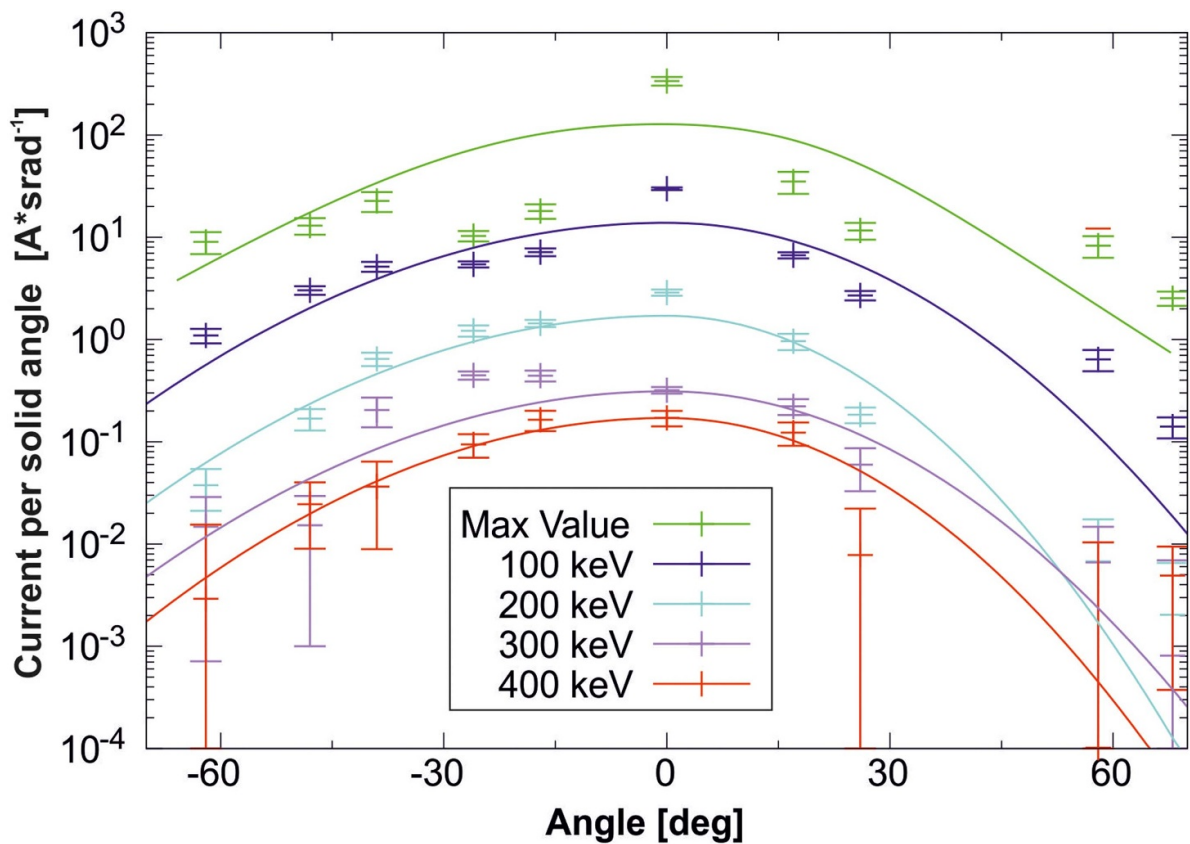


Figure 13. Angular dependence of current of hot electrons emitted from the target in selected intervals around the shown energy levels. The current associated with the slowest electrons observed is shown by the green line marked with the label ‘max value’.

($K\alpha$ data) is close to the number of hot electrons being generated under laser irradiation (polaro-interferometric data). At the same time, the electron spectrometers display a considerably smaller number of hot electrons, although the energy range is quite consistent. The data presented in table 2 may be used for a rough estimate of the total average current of hot electrons outside the plasma region. The values ~ 400 A are about three orders less than the numbers obtained in two other diagnostics. Note, however, that the data from electron spectrometers cannot provide the currents itself: even having

the number and velocity (calculated from energy) of electrons, we do not know their density.

The number of hot electrons measured by optical diagnostics and the $K\alpha$ signal is consistent with the internal currents and may be considered in terms of several models of hot electron production [7, 31–33]. The main mechanisms discussed in the context of the hot electron generation are resonant absorption and parametric instabilities. For the parameters of the current study, the resonant absorption was earlier found to be of great importance and may explain the total number of

Table 2. Deposited laser energy, total electron number, and average electron current for different shots with copper targets obtained from electron spectrometer measurements.

Shot number	Laser energy (J)	Total number of electrons over 4π sr	Average electron current (A/sr)
52 985	481	8.21×10^{11}	375
52 989	458	1.07×10^{12}	490
52 990	516	7.5×10^{11}	343
52 991	464	7.10×10^{11}	325

hot electrons [7]. In [7], the numerical calculations were performed using the ATLANT-HE code, which in axisymmetric geometry provides the solution of the hydrodynamic equations under the inverse bremsstrahlung and resonance absorption mechanisms by taking into account the refraction of laser light. The code calculates the conversion of laser energy absorbed by the resonance mechanism into the energy of hot electrons due to the dissipative process on plasma waves, taking into account the profiling of the density distribution near the plasma resonance region. At the intensity of 10^{16} W cm $^{-2}$ at the first harmonic, the calculations for a plastic target showed the conversion of about 3% of the laser energy into the energy of hot electrons with an average energy of about 70 keV. The significant conversion of the energy of the first harmonic radiation of PALS-laser into the energy of hot electrons, consistent with the presented results, was also measured in the experiments [34–36], devoted to the study of laser energy transfer into the energy of a shock wave propagating in the bulk target.

In the case of the resonant absorption mechanism, the generation of hot electrons occurs along the plasma expansion, and the direction of propagation of plasma waves, which is in general consistent with the observed angular spectra. The stimulated Raman scattering and two-plasmon decay processes [32, 33] generate hot electrons in the direction of the laser radiation incidence on the target and in the transverse direction. So, the angular spread of the hot electron distribution may become rather wide. However, the hot electron distribution is modified self-consistently in the plasma plume to finally have the dominant direction away from the target, as follows from the measured magnetic field orientation (see figure 7(b)) and symmetry of angular distributions in electron spectrometers.

The explanation of the evident difference between the number of hot electrons in the expanding plasma, consistent within optical diagnostics and $K\alpha$ -imaging and the number of the hot electrons detected by electron spectrometers, may shed light on the actual efficiency of the hot electron emission and retention. The effect of suppressing the escape of electrons may be rather strong and at the same time has a complex nonstationary character which in a simplified qualitative manner may be described as follows. At the first stage, plasma expands according to the 1D model proposed in [17, 18]. The fast electrons create a potential jump at the Debye length defined for their characteristic energies ε_e as $r_D \sim \sqrt{\varepsilon_e/4\pi n_e e^2}$, forming a double layer. At this stage, the expansion is 1D, and the field is confined as in a flat capacitor. Here, the ruling parameter is the spatial scale D of the interaction spot, *i.e.* the laser focus size. Once the plasma front with the fast electrons on its edge reaches the scale D , expansion tends to change its geometry

to 3D, and the double layer structure deforms, allowing some of the hottest electrons to escape. A new potential structure is then formed around the charged interaction zone: with almost the velocity of light a discharge pulse propagates in the target material to start charge density reorganization which may compensate the lack of electrons in the expanding plasma. After propagation of the discharge front, the target surface may create a net potential, the value and time evolution of which is defined by the target structure. In the limiting case of a finite mass flat $L \times L$ target free-standing in vacuum, until expanding plasma passes the characteristic scale L of the target the plasma expansion would proceed again in the \sim 1D potential of the charged target.

The plasma expansion on the distance X takes the time of $\tau \sim X/\sqrt{T_e/m_i}$, where T_e is the electron temperature and m_i is the ion mass. If the duration τ corresponding to the size of the target L is not sufficiently longer than the duration of the laser pulse, fast electrons are generated under conditions of strong retention by the potential of the target. Even in the stage of the quasi-spherical expansion, before the plasma radius reaches the characteristic scale of the target surface, which is about 5 mm in the considered setup (see figure 7), the potential where hot electrons are retained is still quasi-1D, provided the expansion is smaller than the light velocity and the laser irradiation is quasi-stationary at this time scale.

To elucidate some features of the electron retention effect at the stage of plasma expansion up to the characteristic target linear size, qualitative 1D particle-in-cell simulations were performed using the code SMILEI [37]. A simulation box of the size of $L_x = 1024 \mu\text{m}$ was filled on its $L_x/3$ with ions (charge state $Z = 3$, mass of 27 proton masses, zero temperature, density $n_0 = 6 \times 10^{22}$ cm $^{-3}$), cold electrons (density of $0.9 Z n_0$ cm $^{-3}$, temperature of 100 eV), and hot electrons (density of $0.1 Z n_0$ cm $^{-3}$, temperature of 50 keV). The resolution was 10 nm in space and 0.02 fs in time. There were 100 particles per cell for each type of electron and 10 particles per cell for ions. The simulation box had an open boundary for particles and fields on the right and reflective on the left. The open boundary allowed electrons to leave the box, particles disappear after the boundary and do not create any electrostatic fields in the simulation box. This quantitatively mimics a switch to 3D expansion, when the electric field is not any more proportional to the electron density. For this simulation, the length scale was in the order of the simulation right edge.

Figure 14 shows that already, from the very first moment, some of the electrons escape the plasma very quickly and go to infinity. It is seen that these are the hottest electrons from the distribution tail, as the electron expansion velocity

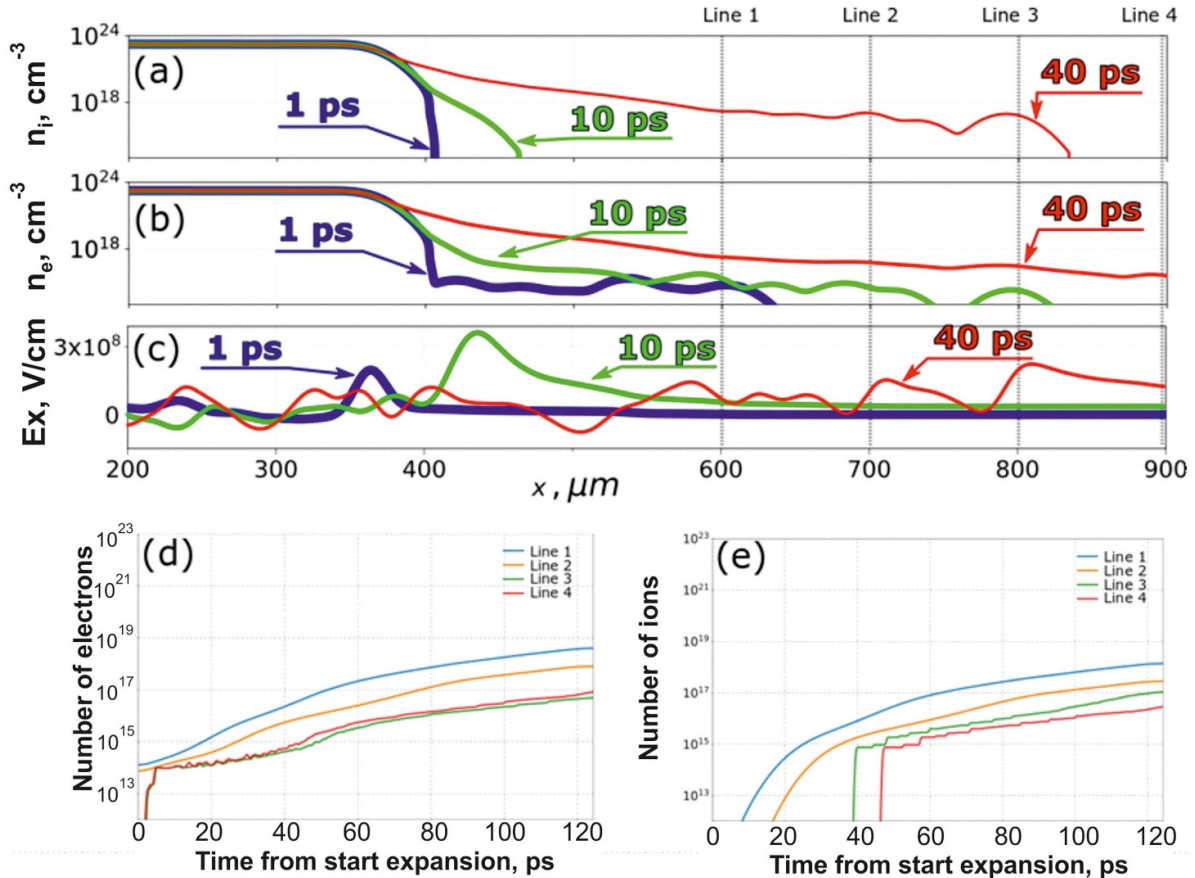


Figure 14. Ion density (panel (a)), electron density (panel (b)), and electrostatic electric field (panel (c)) at 1 ps, 10 ps, and 40 ps after the start of expansion. Two lower panels show temporal dependencies of electron (panel (d)) and ion (panel (e)) number, passing through the lines 1–4 shown in panels (a)–(c).

$v_{eex} \sim \frac{240 \mu\text{m}}{1 \text{ps}} \sim 2.4 \times 10^{10} \text{ cm s}^{-1}$ is of the order of the light velocity. The escaped electrons excite the electrostatic field which in general decelerates the process further. However, the number of escaping electrons is still growing all the time. The maximum electric field scale in the double layer, formed by electrons and ions, is of the order of $E_{\text{max}} \sim \frac{\varepsilon_e}{e r_D}$, according to [18]. However, the direct substitution of electron energy and density gives $E_{\text{max}} \sim 10^{10} \text{ V cm}^{-1}$, the value of about an order of magnitude greater than that in figure 14. This is probably a consequence of a more complex plasma expansion process in the case of two-temperature electron distribution [38]. Comparison of the ion position and electric field profile shows that the field is growing for some time while electrons are still passing to infinity. This is evident for 10 ps; for later times some of the electrons already escaped the box, and the electric field does not further grow noticeably. As we see from panels (a)–(c), the electron current exceeds the ionic one. This is also confirmed by the two lower panels (d) and (e) in figure 14. It indicates that in the simple model introduced above, the three phases of the expansion process are probably strongly overlapping and cannot be separated quantitatively. We may conclude that the electron current in the plasma, *i.e.* up to the distance of 500–600 μm from the surface, is not stopped after the initial fast electron breakthrough. During all the observed time, charge density of electrons passing the flight distances of

600, 700, 800 and 900 μm marked with lines 1–4 is on average slightly greater than that of ions. For the initial parameters of this simulation, where 10% of fast electrons with 50 keV energy was considered, one can extract the value of the current of the order of $\sim 10^{17}$ electrons in ~ 100 ps, which means hundreds of kA. Later, a part of those electrons in 3D would be further decelerated and returned by the target potential, but it is difficult to estimate their fraction from the 1D simulation. Note also that due to technical reasons, in this illustrative simulation the number of hot electrons equals to 10% of the total electron number, and consequently the obtained current is overestimated. For current experimental conditions, the fast electron part is much less, which would scale down the observed current.

Considering the process integrally, the total number of escaped electrons may be estimated as follows. Using the simple model presented above, consider an expanding plasma of radius $R(t)$, increasing in time with a sound velocity [17]. Let the plasma flow from the interaction focal spot with radius r on the target with a characteristic surface scale L . An electric charge of hot electrons may be found from the energy conservation relation as $Q(t) \sim e E_{\text{laser}}(t) * \eta(t) / \varepsilon_e$, where e is the electron charge, $E_{\text{laser}}(t)$ is the laser energy, delivered to the target up to the time moment t , $\eta(t)$ is the conversion efficiency, ε_e is the characteristic energy of hot electrons. The conversion efficiency and characteristic electron

energy are the quantities to be determined considering the laser-plasma interaction. The charge $Q(t)$, which tends to escape the plasma and therefore the target, varies in time. Assume $r \ll R(t) \ll L$, the target is already charged, which corresponds to quasi-spherical expansion, starting very early, according to figure 6. The potential of the target is related to the target charge as $\Phi(t) \sim Q(t)/L$, $L \sim 5$ mm is the target spatial scale in the experiment. The potential $\Phi(t)$ on the other side allows us to relate the number of escaped electrons in expression for $Q(t)$ to their energy as $\varepsilon_e \sim e\Phi(t)$. The estimate for $\varepsilon_e \sim 200$ keV gives the number of electrons $N_e \sim \frac{L\varepsilon_e}{e^2} \sim 7 \times 10^{11}$, consistent with the results in table 2. For the estimated number of electrons N_e and their energies ε_e , the necessary deposited laser energy $E_{\text{laser}}(t)$ transformed into the energy of these electrons is about $E_e \sim N_e\varepsilon_e/\eta \sim 1$ J for absorption efficiency $\eta \approx 0.02$, calculated for the similar parameters in [7]. This estimation shows that the hot electron escape is efficiently suppressed by the electrostatic target potential: in terms of energy it is only a fraction of $E_e/E_{\text{laser}}(\infty) \sim 0.002$. The obtained conclusions on the retention of hot electrons are consistent with the observed data on the electric currents in the spectrometers.

Electrons which are unable to escape deposit their energy and charge back to the target. Depending on their spatial spread, it may happen with different intensities at different distances from the interaction region. Energy deposition results in a continuous heating of the target, for higher electron energies more volumetrically, which is important for all applications involving high energy deposition into the target, such as warm dense matter studies and inertial confinement. Charge deposition is a more transient process. Depending on the target impedance, a discharge process evolves through the target holder. During this discharge, electrons which are yet on the expanding target surface are released, but with much less energy. This process is rather interesting itself and is ruling the physics under optical laser-driven discharge magnetic field generators.

5. Conclusions

In conclusion, by applying multiple diagnostics to characterize the hot electron generation, in the terawatt domain of laser-matter interaction, we have experimentally confirmed that hot electron emission outside the interaction area is strongly suppressed by the electrostatic potential of expanding plasma. The electron flow back to the target contains almost the whole hot electron population. A qualitative estimate which engages the target geometrical factor and electron energies provides a number rather close to the experimental observation. It shows that the process is self-consistent, and on the long-time scales is defined by the integral characteristics of the system, such as the absorbed energy and charge. The general statements of the presented experimental work define conditions for theoretical modelling of hot electron spatial-temporal distributions in numerous high-energy density laser-plasma applications.

Acknowledgments

The authors greatly appreciate discussions with V Tikhonchuk. This research was supported by the Access to the PALS RI under the EU LASERLAB IV project (Grant Agreement No. 654148); by the Ministry of Science and Higher Education, Republic of Poland (Decision no. 3880/H2020/2018/2), by the Ministry of Education, Youth and Sports of the Czech Republic (projects No. LM2015083 (PALS RI) and No.EF16_013/0001552) and by the Czech Science Foundation (Grant Nos. 19-24619S). The work was partially supported by the MEFH Academic Excellence Project (contract No. 02.a03.21.0005, 27.08.2013) and Russian Science Foundation (Project No. 16-11-10174). The work was partially supported by the project # FSWU-2020-0035 (Ministry of Science and Higher Education of the Russian Federation). We acknowledge HPC resources of CINES under allocation 2017-056129 made by Grand Equipment National de Calcul Intensif and resources of NRNU MEFH High-Performance Computing Center. This research has been carried out within the framework of the EUROfusion Enabling Research Project: ENR-IFE19.CEA-01 'Study of Direct Drive and Shock Ignition for IFE: Theory, Simulations, Experiments, Diagnostics Development'. The views and opinions expressed herein do not necessarily reflect those of the European Commission.

Author notes

The authors dedicate this paper to memory of Professor Milan Kalal, who proposed the idea of complex interferometry and its mathematical foundations over 30 years ago. Although this unique method provides extended possibilities and higher reliability compared to classical polaro-interferometry, it has not been effectively used in laser plasma research due to technical difficulties connected with its implementation.

The results of the spontaneous magnetic field measurements presented in this paper have a priority character: they were obtained for the first time using a unique three-frame complex interferometer at the PALS laser facility and confirm the great potential of this method, in accordance with expectations of Prof. Milan Kalal.

ORCID iDs

T Pisarczyk  <https://orcid.org/0000-0002-1109-7683>
 J Krasa  <https://orcid.org/0000-0002-3888-8370>
 J Cikhart  <https://orcid.org/0000-0002-8222-8038>
 G Cristoforetti  <https://orcid.org/0000-0001-9420-9080>
 D Terwińska  <https://orcid.org/0000-0002-0897-0592>
 P Kubes  <https://orcid.org/0000-0003-1356-8765>

References

- [1] Korobkin V V and Serov R V 1966 *JETP Lett.* **4** 70–2
- [2] Stamper J A, Papadopoulos K, Sudan K, Dean S O, McLean E A and Dawson J M 1971 *Phys. Rev. Lett.* **26** 11

- [3] Braginskii S I 1965 Transport processes in a plasma *Reviews of Plasma Physics* ed M A Leontovich (New York: Consultants Bureau) p 205
- [4] Thomson J J, Max. C E and Estabrook K 1975 *Phys. Rev. Lett.* **35** 663
- [5] Basov N G, Wołowski J, Gamali E G, Denus S, Pisarczyk T, Rupasov A A, Sarkisov G S, Sklizkov G B, Tikhonchuk V T and Shikanov A S 1987 Detection of spontaneous magnetic fields in a laser plasma in the "Delfin-1" device *JETP Lett.* **45** 173–6
- [6] Aliev Y M and Bychenkov V M 1979 Parametric generation of magnetic fields by action of strong radiation on a plasma *JETP Lett.* **49** 805–8
- [7] Pisarczyk T *et al* 2017 Kinetic magnetization by fast electrons in laser-produced plasmas at sub-relativistic intensities *Phys. Plasmas* **24** 102711
- [8] Krása J *et al* 2018 Production of relativistic electrons, MeV deuterons and protons by sub-nanosecond terawatt laser *Phys. Plasmas* **25** 113112
- [9] Rusby D R *et al* 2015 Measurement of the angle, temperature and flux of fast electrons emitted from intense laser-solid interactions *J. Plasma Phys.* **81** 475810505
- [10] Rusby D R, Armstrong C D, Scott G G, King M, McKenna P and Neely D 2019 Effect of rear surface fields on hot, refluxing and escaping electron populations via numerical simulations *High Power Laser Sci. Eng.* **7** e45
- [11] Poyé A *et al* 2015 Physics of giant electromagnetic pulse generation in short-pulse laser experiments *Phys. Rev. E* **91** 043106
- [12] Hora H and Eliezer S 1989 Double layers in laser-produced plasmas *Phys. Rep.* **172** 339–407
- [13] Krása J, Klír D, Rezáč K, Cikhardt J, Pfeifer M, Dostál J, Dudžák R and Nassisi V 2019 Target return current in low intensity laser target interaction *Proc. SPIE 11035, Optics Damage and Materials Processing by EUV/X-ray Radiation VII* p 110350G
- [14] Krupka M *et al* 2019 Comprehensive diagnostics of hot electron emission from plasmas produced by sub-nanosecond terawatt laser on thin foil metal targets *JINST* **14** C12003
- [15] Krása J *et al* 2017 Spectral and temporal characteristics of target current and electromagnetic pulse induced by nanosecond laser ablation *Plasma Phys. Control. Fusion* **59** 065007
- [16] Cikhardt J *et al* 2014 Measurement of the target current by inductive probe during laser interaction on terawatt laser system PALS *Rev. Sci. Instrum.* **85** 103507
- [17] Gurevich A V, Pariiskaya L V and Pitaevskii L P 1966 Self-similar motion of rarefied plasma *J. Exptl. And Theoret. Phys.* **49** 647–54
- [18] Mora P 2003 Plasma expansion into a vacuum *Phys. Rev. Lett.* **90** 185002
- [19] Pisarczyk T *et al* 2015 Space-time resolved measurements of spontaneous magnetic fields in laser-produced plasma *Phys. Plasmas* **22** 102706
- [20] Zaras-Szydłowska A, *et al* Complex interferometry application for spontaneous magnetic field determination in laser-produced plasma-P5.214 *44th European Physical Society Conf. on Plasma Physics (26-30 June 2017, Belfast)*
- [21] Kalal M 1991 Complex interferometry: its principles and applications to fully automated on-line diagnostics *Czechoslovak J. Phys.* **41** 743
- [22] Pisarczyk T *et al* 2019 Elaboration of 3-frame complex interferometry for optimization studies of capacitor-coil optical magnetic field generators *J. Instrum.* **14** C11024–24
- [23] Pisarczyk T *et al* 2018 Wavelength dependence of laser plasma interaction related to shock ignition approach *Laser Particle Beams* **36** 405–26
- [24] Dostal J *et al* 2017 Synchronizing single-shot high-energy iodine photodissociation laser PALS and high-repetition-rate femtosecond Ti: sapphire laser system *Rev. Sci. Instrum.* **88** 045109
- [25] Zaras-Szydłowska A 2019 Development of a methodology for amplitude-phase analysis of complex interferograms and its application for the spontaneous magnetic fields measurements in the laser plasma on PALS experiment *Phd Thesis*
- [26] Pisarczyk T, Rupasov A A, Sarkisov G S and Shikanov A S 1990 Faraday-rotation method for magnetic field diagnostic in a laser plasma *J. Sov. Laser Res.* **11** 1
- [27] Renner O, Šmíd M, Batani D and Antonelli L 2016 Suprathermal electron production in laser-irradiated Cu targets characterized by combined methods of x-ray imaging and spectroscopy *Plasma Phys. Control. Fusion* **58** 075007
- [28] Salvat F, Fernandez-Varea J M and Sempau J 2009 Penelope-2008: a code system for monte carlo simulation of electron and photon transport
- [29] Podorov S G, Renner O, Wehrhan O and Förster E 2001 Optimized polychromatic x-ray imaging with asymmetrically bent crystals *J. Phys. D: Appl. Phys.* **34** 2363
- [30] Singh S, Slavicek T, Hodak R, Versaci R, Pridal P and Kumar D 2017 Absolute calibration of imaging plate detectors for electron kinetic energies between 150 keV and 1.75 MeV *Rev. Sci. Instrum.* **88** 075105
- [31] Šmíd M, Renner O, Colaitis A, V T T, Schlegel T and F B R 2019 Characterization of suprathermal electrons inside a laser accelerated plasma via highly-resolved $K\alpha$ -emission *Nat. Commun.* **10** 1–8
- [32] Rosenbluth M N 1972 Parametric instabilities in inhomogeneous media *Phys. Rev. Lett.* **29** 565
- [33] Liu C S, Rosenbluth M N and White R B 1974 Raman and Brillouin scattering of electromagnetic waves in inhomogeneous plasmas *Phys. Fluids* **17** 1211
- [34] Yu. G S *et al* 2006 Efficiency of ablative loading of material upon the fast-electron transfer of absorbed laser energy *Quantum Electron.* **36** 429
- [35] Antonelli L *et al* 2019 Laser-driven strong shocks with infrared lasers at intensity of 10^{16} W/cm² *Phys. Plasmas* **26** 112708
- [36] Gus'kov S Y *et al* 2014 Laser-driven ablation through fast electrons in PALS-experiment at the laser radiation intensity of 1-50 PW/cm² *Laser Particle Beams* **32** 177
- [37] Derouillat J *et al* 2018 SMILEI: a collaborative, open-source, multi-purpose particle-in-cell code for plasma simulation *Comput. Phys. Commun.* **222** 351–73 arXiv:1702.05128
- [38] Bezzerides B, Forslund D W and Lindman E L 1978 Existence of rarefaction shocks in a laser-plasma corona *Phys. Fluids* **21** 2179–85